Comprehensive characterization of atmospheric organic carbon at a forested site

Comprehensive characterization of atmospheric organic carbon at a forested site

James F. Hunter[1,2], Douglas A. Day[3,4], Brett B. Palm[3,4], Reddy L. N. Yatavelli[3,4,5], Arthur W. H. Chan[6,7], Lisa Kaser[8,9], Luca Cappellin[10,11], Patrick L. Hayes[3,4,12], Eben S. Cross[2,14], Anthony J. Carrasquillo[1], Pedro Campuzano-Jost[3,4], Harald Stark[3,4,14], Yunliang Zhao[6,15], Thorsten Hohaus[14,16], James N. Smith[9,17], Armin Hansel[8], Thomas Karl[13], Allen H. Goldstein[6], Alex Guenther[9,18], Douglas R. Worsnop[14], Joel A. Thornton[19], Colette L. Heald[1,20], Jose L. Jimenez[3,4], Jesse H. Kroll[1,21]

[1] Department of Civil and Environmental Engineering, Massachusetts Institute of Technology, Cambridge, MA, USA

[2] Department of Materials Science and Engineering, Massachusetts Institute of Technology, Cambridge, MA, USA

[3] Cooperative Institute for Research in Environmental Sciences, University of Colorado, Boulder, CO, USA

[4] Department of Chemistry and Biochemistry, University of Colorado, Boulder, CO, USA

[5] California Air Resources Board, El Monte, California, USA

[6] Department of Environmental Science, Policy and Management, University of California, Berkeley, CA, USA

[7] Department of Chemical Engineering and Applied Chemistry, University of Toronto, Toronto, Ontario, Canada

[8] Institute for Ion Physics and Applied Physics, University of Innsbruck, Innsbruck, Austria

[9] National Center for Atmospheric Research, Atmospheric Chemistry Observations and Modeling Division, Boulder, CO, USA

[10] Research and Innovation Centre, Fondazione Edmund Mach, S. Michele all'Adige, Italy

[11] School of Engineering and Applied Sciences, Harvard University, Cambridge, Massachusetts, USA

[12] Département de Chimie, Université de Montréal, Montréal, Québec, Canada

[13] Institute of Atmospheric and Cryospheric Sciences, University of Innsbruck, Innsbruck, Austria

[14] Aerodyne Research Inc., Billerica, MA, USA

[15] Department of Mechanical Engineering, Carnegie Mellon University, Pittsburgh, PA, USA

[16] Department of Energy and Climate Research, IEK-8: Troposphere, Forschungszentrum Juelich, Juelich Germany

[17] Department of Chemistry, University of California, Irvine, CA, USA

[18] Department of Earth System Science, University of California, Irvine, CA, USA

[19] Department of Atmospheric Sciences, University of Washington, Seattle, WA, USA

[20] Department of Earth, Atmospheric, and Planetary Science, Massachusetts Institute of Technology, Cambridge, MA, USA

[21] Department of Chemical Engineering, Massachusetts Institute of Technology, Cambridge, MA, USA

Comprehensive characterization of atmospheric organic carbon at a forested site

Atmospheric organic compounds are central to key chemical processes that influence air quality, ecological health, and climate. However, longstanding difficulties in predicting important quantities such as organic aerosol formation and oxidant lifetimes indicate that our understanding of atmospheric organic chemistry is fundamentally incomplete, likely due in part to the presence of organic species that are unmeasured using standard analytical techniques. Here we present measurements of a wide range of atmospheric organic compounds, including previously unmeasured species, taken concurrently at a single site (a ponderosa pine forest during summertime) by five state-of-the-art mass spectrometric instruments. The combined dataset provides a comprehensive characterization of atmospheric organic carbon, covering a wide range in chemical properties (volatility, oxidation state, and molecular size), and exhibiting no obvious measurement gaps. This enables the first construction of a measurement-based local organic budget, highlighting the high emission, deposition, and oxidation fluxes in this environment. Moreover, previously unmeasured species, including semivolatile and intermediate-volatility organic species (S/IVOCs), account for one-third of the total organic carbon, and (within error) provide closure on both OH reactivity and potential SOA formation.

Reactive organic species (carbon-containing compounds other than methane, CO, and CO_2) play a central role in the chemistry of the atmosphere in numerous respects: they can directly impact human and ecosystem health, they influence atmospheric oxidant levels, and their oxidation products include secondary species such as ozone and secondary organic aerosol

(SOA). However, our ability to model such processes is limited by our incomplete understanding of the amount, identity, and chemistry of atmospheric organic compounds. Ambient (field) measurements have revealed a number of large gaps in our understanding of key atmospheric chemical quantities, including secondary organic aerosol[1], total OH reactivity,[2] and total non-methane organic carbon.[3] Such gaps strongly suggest that a substantial fraction of atmospheric organic carbon remains essentially unmeasured and uncharacterized. This places severe limits on our ability to describe the overall lifecycle (emission, reactivity, and loss) and impacts of atmospheric organic compounds. The detection, characterization, and quantification of this unmeasured carbon is thus central for the accurate modeling of air quality, ecological health, and global climate.

However, such measurements are limited by significant analytical challenges. A very large number of organic species are emitted into the atmosphere, and exhibit extraordinary diversity in terms of chemical structure, properties, and reactivity[4]. All are subject to atmospheric oxidation, leading to the formation of new oxidized organic products, exponentially increasing the number and diversity of atmospheric organic species[5]. Volatilities of atmospheric organic compounds span an exceedingly wide range, from volatile organic compounds (VOCs, species present entirely in the gas phase), to intermediate-volatility organic compounds (IVOCs, less volatile species that are still present only in the gas phase), to semivolatile organic compounds (SVOCs, which can be present in both the gas and condensed phases), to extremely low-volatility organic compounds (ELVOCs, which at equilibrium are found almost entirely in the particle phase)[6–8]. This diversity in properties poses detection and quantification challenges since no one instrument is able to measure or characterize all organic compounds in a given sample.

Moreover, S/IVOCs are efficiently lost to inlet/instrument surfaces, and so are not easily measured by standard instrumentation.

Here we describe the first attempt at comprehensive characterization of atmospheric organic carbon, by integrating measurements taken by multiple state-of-the-art mass spectrometric instruments co-located at a montane ponderosa pine forest site. This work expands on earlier compilations of organic carbon measurements[9–11] by including data from several new analytical instruments that target known gaps in analytical measurements (multifunctional species, S/IVOCs), and examining not only the amount of atmospheric organic carbon but also its key properties (volatility, carbon number, and carbon oxidation state). We present measurements of organic species spanning the entire volatility range found in the atmosphere, from VOCs to low-volatility organic aerosol components, over a range of oxidation states, from reduced to highly oxidized. Such comprehensive measurements allow for closure between top-down and bottom-up measurements of OH reactivity (OHR) and SOA formation, and enable the construction of a measurement-based local budget of atmospheric organic carbon.

Concentrations and properties of atmospheric organic species

All measurements were made as part of the BEACHON-RoMBAS field campaign, which took place at the Manitou Experimental Forest Observatory in the Colorado Rocky Mountains in July-August 2011[12]. Data were collected by five instruments, three of which were essentially new to field deployment, and included both speciated techniques (measuring individual compounds) and ensemble techniques (characterizing total amounts and average properties of mixtures). The five instruments were: an Aerodyne time-of-flight aerosol mass spectrometer with thermal denuder (TD-AMS)[13,14], measuring ensemble composition and volatility of organic

aerosol; a proton transfer reaction time-of-flight mass spectrometer (PTR-MS)[15], measuring speciated VOCs; an acetate-ion chemical ionization time-of-flight mass spectrometer with a micro-orifice volatilization impactor (MOVI-CIMS)[16], measuring speciated gas- and particle-phase organic acids; a semivolatile thermal-desorption aerosol gas chromatograph (SV-TAG)[17], measuring speciated and ensemble elutable (nonpolar) semivolatile species; and a thermal desorption electron ionization mass spectrometer (TD-EIMS)[18], measuring ensemble composition and volatility of S/IVOCs. All five instruments utilize a high-resolution time-of-flight mass spectrometer (HTOF-MS, Tofwerk AG), providing measurements of elemental formulas of the ions[13], and hence of elemental ratios[19] and carbon oxidation state ($\overline{OS}_C$)[5]. Further, all instruments provide information on either the carbon number (n_C) of the individual species or the effective saturation vapor concentration (c^*) distribution of the ensemble mixture; one can be estimated from the other from expressions relating carbon number, elemental ratios, and volatility[20,21].

Figure 1 shows the combined measurements from all five instruments, each averaged over its entire measurement period. Diurnal profiles and day vs. night averages are given in the Supporting Information; due to the challenges associated with clearly separating various processes (emissions, photochemistry, transport, etc.), here we focus only on campaign averages. Sampling periods for the instruments did not perfectly overlap, but the relative uniformity of the campaign time series indicates that comparisons of campaign averages over different time periods do not introduce major biases (see SI). Data are presented within two complementary frameworks for representing complex organic mixtures for visualization and modeling, the $\overline{OS}_C$-vs-c^* space[6] (the "two-dimensional volatility basis set", or 2DVBS, Figure 1a), and $\overline{OS}_C$-vs-n_C space[5] (Figure 1b). Major identified compounds are labeled in Fig. 1b; most remaining markers

134 denote species (or ensembles of species) for which the amount and formula (or average formula)
135 are known, but detailed structures are not.

136 Figures 1c-e show the concentration distributions of c^*, n_C, and $\overline{OS}_C$, assuming no
137 overlap between measurements by different instruments (except in unambiguous cases, described
138 in the SI). The summed concentration, 26.7 (25.7-28.6) μgC m^{-3}, represents an upper limit to
139 total observed organic carbon. The lower limit, from assuming maximum overlap among the
140 instruments (see SI), is not substantially different (22.6 (21.7-24.1) μgC m^{-3}), indicating that
141 overlap in measurements by the different instruments does not have a major effect on the total
142 inferred concentrations.

143 As shown in Figure 1, measured organic species span over 19 orders of magnitude in
144 volatility, and exhibit no obvious measurement gaps in any of the dimensions examined. (There
145 are some specific compound classes that may not be measured by this instrument suite; these are
146 likely to be relatively minor, and are discussed in the SI.) Each instrument measures organic
147 compounds in a relatively localized region of chemical space, due to the selectivity of each
148 technique (e.g., the SV-TAG mostly measures low-$\overline{OS}_C$ species, whereas the CIMS mostly
149 measures higher-$\overline{OS}_C$ species), yet overall the measurements are in general agreement. In areas
150 of measurement overlap (e.g. TD-AMS and TD-EIMS), measured values of $\overline{OS}_C$, n_C, and c^* are
151 broadly consistent. This suggests that these five independent instruments provide a self-
152 consistent, and reasonably complete, picture of atmospheric organic carbon.

153 The measurements in Figure 1 include relatively little information about the chemical
154 structures of the organic species; obtaining such information would require the use of additional
155 molecular-level (and possibly offline) techniques, but the present online measurements of the
156 amounts and key ensemble properties (c^*, n_C and $\overline{OS}_C$) still reveal broad trends in the measured

157 organic species, and provide insight into the underlying chemistry of the system. In general,
158 concentrations decrease with decreasing volatility (Figure 1c), increasing carbon number (1d),
159 and increasing oxidation state (1e). The organic carbon is dominated by relatively volatile,
160 reduced compounds – the primary terpenoid emissions 2-methyl-3-buten-2-ol (MBO) and
161 monoterpenes (the spikes in Fig. 2d at n_C=5 and 10) but also small oxygenates (acetone,
162 methanol, etc.), which can be primary or secondary. Most of the remaining carbon is more
163 oxidized than these species and is likely to be products of oxidation reactions. Reactions of
164 primary emissions can lead to decreases in volatility (via functionalization reactions), to form
165 more oxidized, less-volatile gas-phase species (S/IVOCs) and OA. At the same time, the
166 oxidized species tend to have smaller carbon skeletons (lower n_C) as $\overline{OS}_C$ increases (Figure 1b),
167 with the vast majority (96%) made up of molecules with 10 or fewer carbon atoms. Only OA is
168 made up predominantly of larger compounds; thus it may be formed from large precursors (e.g.,
169 sesquiterpenes) and/or oligomerization reactions within the condensed phase. Still, the overall
170 trend of decreasing n_C with increasing $\overline{OS}_C$ suggests the importance of fragmentation reactions
171 during the oxidation of organic species[5]. Such reactions form small, volatile, highly-oxidized
172 species, such as formic and oxalic acids (the spikes in Fig. 2e at $\overline{OS}_C$=+2 and +3), as well as CO
173 and CO_2 (whose production is difficult to observe). This loss to inorganic carbon, as well as to
174 ongoing deposition[23,24], results in the low levels of organic carbon at high values of $\overline{OS}_C$.
175
176 **Total observed organic carbon**
177 The measurements presented in Figure 1 cover a wide and continuous area of chemical
178 space; notably they include S/IVOCs, filling a longstanding measurement gap[25], as well as
179 unspeciated volatile species that are not typically reported. As a result, they cover a substantially

larger fraction of the total organic carbon than has been measured in previous field campaigns. Figure 2a shows organic carbon binned into five major classes, defined by their $\overline{OS}_C$, volatility, and atmospheric lifetime: VOCs (reactive, reduced volatile species), OVOCs (reactive, oxidized volatile organic species), long-lived VOCs (LL-VOCs; less-reactive volatile species, with oxidation lifetimes over 1 day), S/IVOCs (gas-phase species with $c^* \leq 10^7$ μg m^{-3}), and OA (particulate organic carbon). OA accounts for only 4% of the measured organic carbon (1.0 μgC m^{-3}). LL-VOCs are the most abundant, accounting for 40% of the measured organic carbon; this may be underestimated somewhat since small (C_2-C_6) alkanes are not measured. VOCs, OVOCs, and S/IVOCs have somewhat lower and approximately equal carbon mass concentrations. The species reported for the first time in this study – S/IVOCs and unspeciated (O)VOCs – account for 8.7 (8.1-10.3) μgC m^{-3} of organic carbon, which represents 31 (29-35)% of the total observed organic carbon (TOOC). Such species were generally not measured/reported in previous field campaigns, and thus measured organic carbon has been traditionally dominated by speciated VOCs and LL-VOCs. For example, in a series of North American field observations, LL-VOCs generally accounted for ≥50% of TOOC, with limited measurements of OVOCs and virtually no measurements of S/IVOCs[9].

While the present measurements of these species enable the characterization of a larger fraction of atmospheric reactive carbon than has previously been possible, the precise extent of carbon closure cannot be assessed fully, given that total organic carbon (TOC) was not measured. While gas-phase TOC instruments have been used in the past[3,26], they were not deployed in the present campaign. At the same time, TOC measurements as single, scalar quantities may be insufficient for fully describing atmospheric organic carbon, since they

provide no chemical information, and can overlook key low-volatility species (S/IVOCs, OA) that make up a relatively small fraction of the total.

Closure in OH reactivity and potential SOA formation

Nonetheless, the completeness of the measured suite of organic compounds, and the importance of previously-unmeasured species (S/IVOCs and unspeciated (O)VOCs), can be assessed by examining closure for two key atmospheric quantities, OHR and SOA formation. Such closure involves comparson of measurements of the total quantity of interest ("top-down") with the sum of estimated contributions from all individual measured species ("bottom-up"); in most previous studies, for both OHR and SOA formation the bottom-up approach generally underestimates the total, often by a substantial amount[1,2].

OHR is computed from measured concentrations and known/estimated OH rate constants (see Methods). Contributions to OHR from each component (using the upper-limit measurements of organic carbon, Figure 2a) are given in Figure 2b. Reactivity is dominated by MBO and reactive terpenoids (isoprene and monoterpenes); these account for 16% of TOOC but 62% of the total OHR, and thus dominate local photochemical activity. The LL-VOCs, a set of small oxygenated VOCs dominated by acetone, methanol, and formic acid, make up only a small fraction (3%) of reactivity despite their large (40%) contribution to TOOC. Unspeciated (O)VOCs and S/IVOCs account for the remaining 25%; this represents a significant, and usually unmeasured, component of OH reactivity. Summed OH reactivity from all measured components is 7±1 s^{-1} (Using the lower-limit concentrations gives a value of 6±1 s^{-1}.) Total (ensemble) OH reactivity was not measured during this campaign, but was found to be 10 s^{-1} at the same site the previous summer[27]. After adjusting for differences in emissions between the two summers (see

SI), this corresponds to a value of 8±1 s^{-1} for the present campaign. The agreement between bottom-up and top-down determinations of OH reactivity suggests that the previously-unmeasured compounds quantified in this work (S/IVOCs and unspeciated (O)VOCs) are sufficient to account for the missing OH reactivity at this site. In fact, our measurement of a 25% contribution by these species to OH reactivity agrees well with the estimated 30-40% contribution from unmeasured compounds from this site in previous years[27,28].

Top-down measurements of the amount of SOA that can be generated from the OH-initiated oxidation of ambient organic compounds were made using an oxidation flow reactor (OFR), which exposes ambient air to high levels (3.9-15 × 10^8 molecules/cm^3) of OH radicals, under conditions in which RO_2+HO_2 reactions dominate[29]. OA formation was always observed; after correction for various loss processes in the reactor (see SI), the campaign-average maximum increase in OA carbon was 0.9 (0.6-1.2) μgC/m^3. Contributions from individual components, estimated from measured concentrations multiplied by carbon yields (from laboratory studies or estimates, as discussed in Methods) are shown in Figure 2c. Total SOA formation is calculated to be 1.4 (1.2-2.0) μgC/m^3, using the upper-limit measurements, or 0.8 (0.6-1.4) μgC/m^3 using the lower-limit measurements; this range is in agreement with the OFR measurements, providing closure (within error) in potential SOA formation. The measured S/IVOCs are critical to this closure, accounting for a large fraction, 78% (74-85%), of the total SOA formation. This highlights the importance of S/IVOCs as SOA precursors; without them, SOA formation from the other measured species is calculated to be only 0.32 (0.29-0.35) μgC m^{-3}, far less than was observed.

Local organic carbon budget

248 The present measurements, combined with calculated reaction rates and estimates of
249 emission[30] and deposition fluxes[23,31], enable the first construction of an observationally-based
250 local budget for atmospheric organic carbon, shown in Figure 3. Details of these calculations are
251 given in the Methods section.
252 Reactive BVOCs dominate the emission of organic carbon (though LL-VOCs are also
253 major contributors). Once emitted, BVOCs oxidize to form a range of products: OVOCs, OA,
254 LL-VOCs, and CO/CO_2. The fate of OVOCs and OA is more complex, since these organic
255 classes may undergo deposition and gas-particle partitioning, as well as oxidation to form other
256 compounds of the same type. (Because of such recycling reactions, denoted by curved arrows,
257 the total flux out of a given category does not necessarily equal the total flux in.) Depositional
258 loss of carbon, while uncertain, is dominated by OVOCs and S/IVOCs, consistent with previous
259 work[23,24]. The LL-VOC carbon is largely a "dead end" with respect to the local oxidation
260 chemistry, since this pool contributes relatively little to the reactivity or SOA formation at the
261 site (Fig. 2). On the timescales accessed in this study (minutes to hours after emission), LL-
262 VOCs are therefore similar to inorganic oxidation products (CO and CO_2). By contrast, most of
263 the remaining species (BVOCs, OVOCs, and S/IVOCs) are associated with large oxidation and
264 deposition rates, indicating that such reactive organic carbon is highly dynamic, with average
265 lifetimes of no more than a few hours.
266 At the same time, most of these rates are highly uncertain (with typical uncertainties of
267 >50%), or are even completely unconstrained. This highlights our low level of understanding of
268 the processes that govern the atmospheric lifecycle of organic carbon (emission, deposition, and
269 oxidation), and the need for improved constraints on these rates. Centrally important are the
270 product distributions of the oxidation reactions; these include not only the branching among

271 different product classes (e.g., the yields of OVOCs, OA, LL-VOCs, and CO/CO_2 from VOC
272 oxidation), but also how molecular species or classes change upon oxidation (i.e., their
273 movement through the 2D spaces in Figure 1), which is poorly constrained at present. Similarly,
274 while the additional organic carbon measured/reported in this work appears to be sufficient,
275 within error, to close longstanding gaps in OH reactivity and SOA formation (Figs 2b-c), the
276 errors in such estimates remain substantial. These arise predominantly from uncertainties in
277 oxidation rate constants and SOA yields of the unspeciated compounds.
278 This work thus points to the continuing need for additional process-based (laboratory)
279 studies of the transformation of atmospheric organic carbon from one form to another, using the
280 same types of measurements used in the present field study (ideally in conjuction with more
281 detailed measurements of chemical speciation and structure). These can provide important
282 constraints on the rates, branching, and product distributions of key organic species and classes,
283 particularly those that have not been measured routinely until now. Additionally, this work
284 emphasizes the need for an improved understanding of the coupling of chemistry and dynamics
285 (e.g., timescales of chemical reaction vs. deposition vs. transport) when interpreting field
286 observations and assessing the lifecycle of atmospheric organic carbon.
287

References.

1. Hallquist, M. *et al.* The formation, properties and impact of secondary organic aerosol: current and emerging issues. *Atmos. Chem. Phys.* **9,** 5155–5236 (2009).

2. Yang, Y. *et al.* Towards a quantitative understanding of total OH reactivity: A review. *Atmos. Environ.* **134,** 147–161 (2016).

3. Chung, M. Y., Maris, C., Krischke, U., Meller, R. & Paulson, S. E. An investigation of the relationship between total non-methane organic carbon and the sum of speciated hydrocarbons and carbonyls measured by standard GC/FID: Measurements in the Los Angeles air basin. *Atmos. Environ.* **37,** S159–S170 (2003).

4. Goldstein, A. H. & Galbally, I. E. Known and Unexplored Organic Constituents in the Earth's Atmosphere. *Environ. Sci. Technol.* **41,** 1514–1521 (2007).

5. Kroll, J. H. *et al.* Carbon oxidation state as a metric for describing the chemistry of atmospheric organic aerosol. *Nat. Chem.* **3,** 133–9 (2011).

6. Donahue, N. M., Kroll, J. H., Pandis, S. N. & Robinson, A. L. A two-dimensional volatility basis set – Part 2: Diagnostics of organic-aerosol evolution. *Atmos. Chem. Phys.* **12,** 615–634 (2012).

7. Donahue, N. M., Robinson, A. L., Stanier, C. O. & Pandis, S. N. Coupled Partitioning, Dilution, and Chemical Aging of Semivolatile Organics. *Environ. Sci. Technol.* **40,** 2635–2643 (2006).

8. Ehn, M. *et al.* A large source of low-volatility secondary organic aerosol. *Nature* **506,** 476–479 (2014).

9. Heald, C. L. *et al.* Total observed organic carbon (TOOC) in the atmosphere: a synthesis

of North American observations. *Atmos. Chem. Phys.* **8,** 2007–2025 (2008).

10. de Gouw, J. A. *et al.* Budget of organic carbon in a polluted atmosphere: Results from the New England Air Quality Study in 2002. *J. Geophys. Res.* **110,** D16305 (2005).

11. Koss, A. R. *et al.* Photochemical aging of volatile organic compounds associated with oil and natural gas extraction in the Uintah Basin, UT, during a wintertime ozone formation event. *Atmos. Chem. Phys.* **15,** 5727–5741 (2015).

12. Ortega, J. *et al.* Overview of the Manitou Experimental Forest Observatory: site description and selected science results from 2008 to 2013. *Atmos. Chem. Phys.* **14,** 6345–6367 (2014).

13. DeCarlo, P. F. *et al.* Field-Deployable, High-Resolution, Time-of-Flight Aerosol Mass Spectrometer. *Anal. Chem.* **78,** 8281–8289 (2006).

14. Huffman, J. A., Ziemann, P. J., Jayne, J. T., Worsnop, D. R. & Jimenez, J. L. Development and characterization of a fast-stepping/scanning thermodenuder for chemically-resolved aerosol volatility measurements. *Aerosol Sci. Technol.* **42,** 395–407 (2008).

15. Graus, M., Müller, M. & Hansel, A. High resolution PTR-TOF: Quantification and formula confirmation of VOC in real time. *J. Am. Soc. Mass Spectrom.* **21,** 1037–1044 (2010).

16. Yatavelli, R. L. N. *et al.* A Chemical Ionization High-Resolution Time-of-Flight Mass Spectrometer Coupled to a Micro Orifice Volatilization Impactor (MOVI-HRToF-CIMS) for Analysis of Gas and Particle-Phase Organic Species. *Aerosol Sci. Technol.* **46,** 1313–1327 (2012).

17. Zhao, Y. *et al.* Development of an In Situ Thermal Desorption Gas Chromatography

Instrument for Quantifying Atmospheric Semi-Volatile Organic Compounds. *Aerosol Sci. Technol.* **47,** 258–266 (2013).

18. Cross, E. S. *et al.* Online measurements of the emissions of intermediate-volatility and semi-volatile organic compounds from aircraft. *Atmos. Chem. Phys.* **13,** 7845–7858 (2013).

19. Canagaratna, M. R. *et al.* Elemental ratio measurements of organic compounds using aerosol mass spectrometry: characterization, improved calibration, and implications. *Atmos. Chem. Phys.* **15,** 253–272 (2015).

20. Daumit, K. E., Kessler, S. H. & Kroll, J. H. Average chemical properties and potential formation pathways of highly oxidized organic aerosol. *Faraday Discuss.* **165,** 181 (2013).

21. Pankow, J. F. & Asher, W. E. SIMPOL.1: a simple group contribution method for predicting vapor pressures and enthalpies of vaporization of multifunctional organic compounds. *Atmos. Chem. Phys.* **8,** 2773–2796 (2008).

22. Donahue, N. M., Epstein, S. A., Pandis, S. N. & Robinson, A. L. A two-dimensional volatility basis set: 1. organic-aerosol mixing thermodynamics. *Atmos. Chem. Phys.* **11,** 3303–3318 (2011).

23. Nguyen, T. B. *et al.* Rapid deposition of oxidized biogenic compounds to a temperate forest. *Proc. Natl. Acad. Sci.* **112,** E392–E401 (2015).

24. Park, J.-H. *et al.* Active Atmosphere-Ecosystem Exchange of the Vast Majority of Detected Volatile Organic Compounds. *Science.* **341,** 643–647 (2013).

25. Robinson, A. L. *et al.* Rethinking Organic Aerosols: Semivolatile Emissions and Photochemical Aging. *Science.* **315,** 1259–1262 (2007).

26. Roberts, J. M., Bertman, S. B., Jobson, T., Niki, H. & Tanner, R. Measurement of total nonmethane organic carbon (C_y): Development and application at Chebogue Point, Nova Scotia, during the 1993 North Atlantic Regional Experiment campaign. *J. Geophys. Res.* **103,** 13581 (1998).

27. Kim, S. *et al.* Evaluation of HO_x sources and cycling using measurement-constrained model calculations in a 2-methyl-3-butene-2-ol (MBO) and monoterpene (MT) dominated ecosystem. *Atmos. Chem. Phys.* **13,** 2031–2044 (2013).

28. Nakashima, Y. *et al.* Total OH reactivity measurements in ambient air in a southern Rocky mountain ponderosa pine forest during BEACHON-SRM08 summer campaign. *Atmos. Environ.* **85,** 1–8 (2014).

29. Palm, B. B. *et al.* In situ secondary organic aerosol formation from ambient pine forest air using an oxidation flow reactor. *Atmos. Chem. Phys.* **16,** 2943–2970 (2016).

30. Kaser, L. *et al.* Undisturbed and disturbed above canopy ponderosa pine emissions: PTR-TOF-MS measurements and MEGAN 2.1 model results. *Atmos. Chem. Phys.* **13,** 11935–11947 (2013).

31. Hodzic, A. *et al.* Volatility Dependence of Henry's Law Constants Of Condensable Organics: Application to Estimate Depositional Loss of Secondary Organic Aerosols. *Geophys. Res. Lett.* **41,** 4795–4804 (2014).

Corresponding Author: Correspondence and requests for materials should be addressed to J.H.K. (jhkroll@mit.edu)

Acknowledgments.

Compilation of the multi-instrument data was supported by NOAA grant NA10OAR4310106. Contributions from individual researchers were supported by NOAA NA10OAR4310106 (J.F.H., E.S.C., A.J.C., and J.H.K.); NSF ATM-0919189, NSF AGS-1243354, and DOE DE-SC0011105 (D.A.D., R.L.N.Y., P.L.H., B.B.P., P.C.-J., H.S., J.L.J.); US EPA STAR Graduate Fellowship FP-91761701-0 (B.B.P.); NSF RAPID 1135745 (A.W.H.C., Y.Z., A.H.G.); the Drefyus Foundation (E.S.C.); Austrian Science Fund (FWF) project number L518-N20 (A.H, L.K.) DOC-FORTE-fellowship of the Austrian Academy of Science (L.K.) and NSF AGS-1238109 (C.L.H.). The SV-TAG, CIMS, and TD-EIMS were developed with support from the DOE SBIR program, grants DE-FG02-08ER85160, DE-FG02-08ER85160, DE-SC0004577, and DE-SC0001666. The authors are grateful to Andrew Turnipseed and the management of the Manitou Experimental Forest Observatory for field support, to Nicole Grossberg and Barry Lefer for their measurements of boundary layer heights, to Nathan Kreisberg and Susanne Hering for their development and support of the SV-TAG, and and to Allison Steiner for helpful discussions regarding vertical mixing.

Author Contributions.

Instrument deployment, operation, and data analysis were carried out by: J.F.H, E.S.C, A.J.C., and J.H.K. (TD-EIMS); R.L.N.Y., D.A.D, H.S., J.A.T., and J.L.J (CIMS); P.L.H., B.B.P., D.A.D., P.C.-J., and J.L.J. (TD-AMS); L.K., L.C., A.H., and T.K. (PTR-MS); A.W.H.C., Y.Z.,

and A.H.G. (SV-TAG). D.A.D. organized the BEACHON-RoMBAS field campaign along with J.N.S., A.G., and J.L.J. J.F.H. and D.A.D. compiled the multi-instrument data; J.F.H, D.A.D, D.R.W, C.L.H, J.L.J., and J.H.K, interpreted the compiled dataset. J.F.H. and J.H.K. wrote the paper. All authors commented on the manuscript.

Competing Financial Interests. The authors declare no competing financial interests.

406 **FIGURE CAPTIONS**

407

408 **Figure 1**: Campaign-average measurements of non-methane organic carbon loadings and
409 properties during BEACHON-RoMBAS, colored by the analytical teachnique used (see legend).
410 Panels a and b: plots of carbon oxidation state ($\overline{OS}_C$) vs. volatility (c^* at 298K, μg m^{-3}) and
411 carbon number (n_C), respectively; circle area is proportional to total carbon mass. Panels c-e
412 show the projections onto the three unique axes in panels a and b, assuming minimal overlap
413 between the organic species measured by each instrument (see text). Determination of error bars
414 (1σ) is described in the Methods section.

415

416 **Figure 2.** Observed organic carbon concentrations, OHR, and SOA formation, colored by
417 instrument and organized into major classes of organic species. Gas-phase species are classified
418 into four categories: LL-VOCs (τ>1d), S/IVOCs (τ≤1d, and $c^* \leq 10^7$ μg m^{-3}), VOCs (τ ≤1d, $c^* > 10^7$
419 μg m^{-3}, and $\overline{OS}_C$<-1), and OVOCs (τ<1d, $c^* > 10^7$ μg m^{-3}, and $\overline{OS}_C \geq$-1); error bars, summed for
420 each category, are 1σ. Unlabeled boxes indicate unidentified species or ensemble measurements.
421 It is assumed there is no overlap in measurements by different instruments, so all values represent
422 upper limits. Values of OHR and SOA are calculated as described in the Methods section.

423

424 **Figure 3.** Observationally-constrained budget of atmospheric reactive carbon in the study region,
425 based on campaign-averaged loading measurements and estimated rates of emission, deposition,
426 and oxidation. Units are in μgC m^{-3} (loadings) and μgC m^{-3} hr^{-1} (rates); all errors are 1σ. Organic
427 classes are simplified from those in Figure 2, with VOCs and sesquiterpenes combined into a single
428 BVOC category, and S/IVOCs and OVOCs combined. Arrow color denotes type of process: red

– oxidation; blue – emission/deposition; grey – other physical processes (transport, dilution, partitioning). Dashed arrows denote processes for which rates are largely unconstrained. Calculation details are given in Methods.

METHODS

Details of the sampling site. Measurements were made at the Manitou Experimental Forest in the Colorado Rocky Mountains, as part of the "Bio-hydro-atmosphere interactions of Energy, Aerosols, Carbon, H2O, Organics & Nitrogen – Rocky Mountain Biogenic Aerosol Study" (BEACHON-RoMBAS), running 15 July to 30 August, 2011. The site is located at 2370 m elevation in the Colorado Rockies, 40 km northwest of Colorado Springs and 70 km southwest of Denver, CO (39.10 N, 105.10 W), in a ponderosa pine plantation surrounded by forests with pine, other conifers, and aspen. Details of the site and measurements are described by Ortega et al.[12]

Instruments and data analysis.

All mass spectrometric measurements used for this analysis were ground-based, with the five instruments located in four temperature-controlled trailers. Sampling height was 25 m for the PTR-MS and 4-5 m for the other instruments.

Thermal Denuder – Aerosol Mass Spectrometer (TD-AMS). A high-resolution time-of-flight AMS (Aerodyne Research Inc., Billerica, MA)[13] sampled air downstream of a thermal denuder[14] for 5 minutes every 30 minutes from 20 July to 2 Aug and 9 to 30 Aug. The temperature was cycled from ~20 °C to 250 °C and back to ~20 °C every two hours. The AMS quantifies total OA for submicron non-refractory particles, and provides calibrated elemental ratios using high-resolution peak fitting, with an empirical correction for biases arising from molecular thermal decomposition and ion fragmentation[19]. For additional details of operation, calibration, and analysis of the HR-ToF-AMS and alternating sampling configuration, see Palm

et al.[29] The *c** mass distribution was calculated following the empirical method of Faulhaber et al.[32] Error in the OC measurement is 40%, based on errors from total organic mass[33] and from elemental ratio determinations[19].

Thermal Desorption – Electron Ionization Mass Spectrometer (TD-EIMS). Thermograms of S/IVOC mass spectra were collected every ~11 minutes using the Thermal Desorption Electron Ionization mass spectrometer (TD-EIMS)[18]. The instrument uses cryogenic trapping of the sample followed by temperature-programmed desorption to determine mass concentrations and bulk chemical composition (approximate elemental composition) as a function of volatility, calibrated using *n*-alkanes with known vapor pressures, and reported from log(*c**) = 1 to 7. The TD-EIMS operated for a total of 8 days (26 July, 28 to 29 July, and 8 to 12 Aug), collecting 794 individual desorptions. Error in the OC measurement from the TD-EIMS is estimated to be a factor of three in each volatility bin, accounting for variations in collection, desorption, and detection efficiencies for the range of compounds expected in the ambient environment. This reduces to an error of +75%/-25% for the sum of the volatility bins. The instrument precision during α-pinene calibrations is much better (~0.75 μg/m^3 over the calibration range of 5-15 μg/m^3), arising from variability in the collection, desorption and background on a run-to-run basis. Applying this to the ambient average of 3.1 μg/m^3 gives an error of 28%. Additional details of the calibration procedures and analysis are given in the SI.

Micro-Orifice Volatilization Impactor – Chemical Ionization Mass Spectrometer. A high-resolution time-of-flight mass spectrometer (MOVI-CIMS, Aerodyne Research Inc., Billerica, MA) using the acetate (CH_3COO^-) reagent ion was used to selectively detect gas and particle-phase organic acids[16]. The MOVI interface allows for both gas-phase analysis during aerosol collection on a stainless steel post and thermal desorption of collected aerosol in ultra-high purity

N_2. Data were collected from 20 Aug to 30 Aug at a time resolution of ~1.5 hours, yielding a single gas and particle-phase mass spectrum every sampling/analysis cycle. These mass spectra are used for multi-peak fitting yielding identification (elemental formula) and quantifications of 1374 molecular ions, attributed to acids[34]. Due to the possibility of thermal decomposition of thermolabile species[35,36], particle-phase data are reported as a volatility-resolved ensemble, rather than as individual species. Particle-phase concentrations were calculated using background-subtracted average thermograms of all organic ions (containing C, H, O, and N) identified in the high-resolution mass spectra. Conversion from peak desorption temperature to saturation concentration (c^*) was achieved by measuring calibration thermograms of mixtures of 4 organic acids[37]. The average thermograms were then fitted to a set of basis functions, whose shapes and positions were determined by the calibration measurements. They areas of these peaks yielded the volatility distributions. To obtain elemental ratios, average thermograms of total signal for O, H, and C were calculated. Average n_C values for individual volatility bins were calculated using the same methods as for the TD-AMS and TD-EIMS. This results in a larger particle-phase concentration and organic acid fraction of OA (48%) than has been previously reported (29%) for the dataset[38], but increases sensitivity to fragment ions resulting from desorption of thermolabile, low-volatility molecules. Measurement error is 5% for known, calibrated compounds. For unknown/uncalibrated compounds, error is estimated to be a factor of three based on the range in calibration slopes of known acids. Applying this error to the individual unknown ions and adding in quadrature gives an ensemble error of 35%. Additional details on instrument configuration, data collection, background subtraction, and data analysis are given elsewhere[38,39].

Proton Transfer Reaction Time-of-Flight Mass Spectrometer (PTR-MS). The time-of-flight PTR-MS (IONICON Analytik, Innsbruck, Austria)[15] collected data from 19 July to 9 Aug. Details of instrument configuration, operation, and calibration are described in Kaser et al.[40] High-resolution peak fitting was performed on 30-second averaged raw spectra, fitting 513 peaks in the range *m/z* 14-391, yielding both signal intensity and elemental formula. Background spectra were fit separately, spectra were then averaged to 1 hour, and then background spectra were subtracted after ion fitting. Ion signals were converted to concentrations using in-field standard calibrations for 10 compound gases and an average sensitivity for the remainder of peaks. For this analysis, only the 305 compounds containing at least one carbon atom were used. $C_5H_9^+$ ion signal was assigned to MBO (which is primarily measured as $C_5H_{11}O^+$) and isoprene in a 9:1 ratio, based on previous work at the site[30]; $C_3H_7O^+$ was assigned entirely to acetone and $C_2H_5O_2^+$ to acetic acid (rather than propanal and glycolaldehyde, respectively), given the large emissions and long lifetimes of those species. For known (calibrated) compounds, error in measured concentrations is 10%. For unknown ions, concentrations were calculated using a relative rate approach with a calibration compound[41]. This contributes an error of 30% per ion, leading to an ensemble error of ~8% when added in quadrature.

Semivolatile Thermal-Desorption Aerosol Gas Chromatograph-Mass Spectrometer (SV-TAG). S/IVOCs were measured by the semivolatile thermal desorption aerosol gas-chromatograph/aerosol mass spectrometer (SV-TAG-AMS) from 19 to 30 Aug. The details of the instrument are described in Chan et al.[42] In brief, compounds are collected on a metal fiber filter cell for 90 minutes, and thermally desorbed in helium carrier gas to a gas chromatography/mass spectrometer (GC/MS). Authentic standards and deuterated internal standards are used for mass calibration and quantification. A large number of individual species

were detected and quantified, but these made up a negligible fraction of TOOC and so here only ensemble measurements (binned by volatility) are reported. Ion signals are separated by their elemental formulas ($C_xH_yO_z^+$) and the hydrocarbon ions ($C_xH_y^+$) quantified using a set of analytical standards[42]. The total ion chromatogram is divided into decadal volatility bins based on the measured retention times and known vapor pressures of *n*-alkanes. Error in measured OC is estimated to be 60%, based on the range of calibration factors found for standards within any individual *c** bin.

Determination of $\overline{OS}_C$, n_C, and *c.** For all instruments, the average carbon oxidation state (of individual species or the ensemble) is determined from the formula $\overline{OS}_C = 2\ O/C - H/C$ [5]. The presence of peroxide groups and reduced nitrogen introduces some errors into this calculation, but unless these moieties are extremely abundant, these errors are small[5]. CIMS and AMS measurements suggest that nitrogen-containing organic species are present in very low abundances (N/C<0.03) at this site[34,43]. For the ensemble electron ionization instruments (TD-AMS, TD-EIMS, TAG) elemental ratios may be biased by ion fragmentation; however such biases introduce little error to the determination of $\overline{OS}_C$[19].

Each instrument also provides measurements of n_C (speciated measurements: CIMS(g), PTR-MS) or *c** (ensemble, thermally-separated measurements: TD-AMS, TD-EIMS, CIMS(p), SV-TAG), requiring determination of the remaining quantity. For identified organic species (e.g., simple VOCs, OVOCs, and LL-VOCs), literature *c** values[44] are assigned. For other compounds measured by speciated techniques, *c** is estimated from the SIMPOL structure-activity relationship[21], assuming an alkane carbon skeleton and functional groups based on the measured number of oxygen atoms and the best estimate for the functional groups measured. For the

CIMS, the first two oxygen atoms are assigned to an acid group and the remaining ones to hydroxyl groups, an approach that leads to the strongest agreement between measured and calculated partitioning[39]. For the PTR-MS, oxygen atoms are assigned to carbonyl groups, since molecules with hydroxyl moieties tend to be lost in the unheated inlet of the instrument or to dehydrate upon ionization. In the latter case, this approach may lead to errors in c^* (but not in $\overline{OS}_C$); this effect is difficult to quantify but is unlikely to affect overall results significantly. For the TD-EIMS, TD-AMS, and the SV-TAG, for which c^* distributions are measured, average values of n_C are determined using the approach of Daumit et al.[20], assigning a functional group distribution from measured values of c^*, O/C, and H/C. This approach assigns all double bond equivalents to carbonyl groups, so the presence of C=C double bonds or rings would lead to a modest overestimate in n_C; however the presence of other common functional groups (e.g., peroxides, nitrates) is unlikely to introduce substantial errors in this approach[20]. The high temperatures associated with measurements of low-volatility species (OA and S/IVOCs, as measured by the TD-AMS, TD-EIMS, SV-TAG, and MOVI-CIMS) may lead to thermal decomposition of oligomeric (and other thermolabile) species. In these cases the derived c^* and n_C values correspond not to the exact values of the ambient species but instead to effective values associated with both physical partitioning and chemical reaction[35,36].

Reactivity calculations. OH reactivity (Figure 2b) and reaction rates of the organic species (Figure 3) were estimated based on rates of reactions with OH, O_3, and NO_3 as well as photolysis. For rate calculations, diurnally averaged concentrations of [OH]=2.0×10^6 molec cm^{-3} [27], [O_3]=9.8×10^{11} molec cm^{-3} [12], and [NO_3]=4.9×10^6 molec cm^{-3} [43] were used. Rate coefficients were taken from the literature when available (see Table S1), and a 30% uncertainty is assumed.

For unidentified species, oxidation is assumed to be driven by H-atom abstraction by OH, with rate coefficients estimated using the relationship given by Donahue et al.[45] This method accounts for differences in the rate coefficient due to the number of carbon, hydrogen, and hydrogen atoms, as well as the "trapping effect," wherein oxidation slows for lower-volatility compounds partitioned in the condensed phase. A factor of three uncertainty is used for these estimated OH rate coefficients. If C=C double bonds are an abundant moiety in the unidentified species, oxidation rates (due to reaction with OH, NO_3, or O_3) may be substantially faster. Unfortunately, given the importance of cyclic structures in biogenic species, the abundance of C=C bonds cannot be determined from the present measurements.

SOA formation calculations. The aerosol mass formed after oxidation (Figure 2c) was calculated from measured SOA carbon yields, assuming this is the maximum SOA formed from a given precursor. Oxidative processes that are likely to be unimportant within the OFR, such as aqueous-phase oxidation, were not considered. For compounds whose SOA yields have been measured in the laboratory at ambient OA loadings (and low-NO_x conditions), literature mass yield values were used, and converted to carbon yields using measured OM/OC values (see SI). Error is estimated to be 30%. For the remainder of the compounds, carbon yield was parameterized using an approach similar to that of Donahue et al,[46] in which yield is a function of the c^* of the precursor. Details of this parameterization are given in the SI; uncertainty in these yields is estimated to be a factor of three.

Flux calculations. Emission fluxes of the dominant VOCs, OVOCs and LL-VOCs were taken from flux measurements made at the same site during the previous summer[30,47]. These were

592 taken at nearly the same time of year (3 Aug to 8 Sept, 2010); photosynthetically-active radiation
593 (PAR) was slightly higher and temperature was on average 2°C lower than the present (2011)
594 measurements (see Fig. S2). This leads to increased fluxes in 2011 for all species except MBO,
595 which decreased slightly (differences were calculated using the equations given in Kaser et al.[30]).
596 Flux measurements were of fluxes out of the canopy, meaning that the amount of VOCs that
597 react below the canopy must also be accounted for. This component is estimated by multiplying
598 the measured VOC reaction rate by the average canopy height (16 m), which assumes relatively
599 rapid transport of air out of the canopy. This is added to the out-of-canopy flux to determine the
600 total flux, and then the result divided by the average boundary layer height to determine the
601 column average reaction rate. Although the adjustment for differences in temperature and
602 radiation is fairly robust, it is possible that other differences between 2010 and 2011 (such as
603 rainfall) could lead to differences in the emissions between the two years. Additionally, the
604 measured fluxes are restricted to a relatively small number of compounds with concentrations
605 large enough to be measureable. Because about half of the reactive carbon is made up of
606 unidentified compounds with small concentrations, it is possible that the fluxes could be up to a
607 factor of two larger. This positive error is included in the BVOC flux in Figure 3.
608 Oxidation rates were determined using one of two methods, depending on the lifetime of
609 the species. For species whose overall lifetimes are sufficiently long relative to the mixing
610 timescale (1.5 hours on average; see SI), they are treated as vertically well-mixed, and oxidation
611 rate ($\mu g\ m^{-3}\ hr^{-1}$) is determined by dividing concentration by oxidative lifetime. Shorter-lived
612 species, namely the primary biogenic VOCs (daily average lifetime ~1.2 hr) are likely not well-
613 mixed, and thus their ground-level concentrations are unlikely to be representative of the average
614 concentration in the mixed layer. Instead, these short-lived species are assumed to be in steady-

state, so that their reactive rate can be assumed to be equal to the total emission rate (described above). Uncertainties in oxidation rates (Fig. 3) are calculated from estimated rate coefficients, as described above.

Deposition fluxes were estimated using the approach described by Hodzic et al.[31] The deposition velocities estimated in this way range from 0 for volatile species and plateau at 4 cm/s for low-volatility species. These estimated velocities are qualitatively similar to measured deposition velocities reported by Nguyen et al.[23], who found peak velocities in the 1-5 cm/s range for a variety of organic and inorganic molecules. The daily average deposition velocity for formic acid in Nguyen et al. was approximately 0.5 ± 0.2 cm/s, which is somewhat higher than the calculated value of 0.14 cm/s used in this study. This difference is likely due to a combination of errors in the calculation methods, and real differences in the two field sites and meteorological conditions. Particle dry deposition velocities were not measured at this site and so were taken from Zhang et al.[48], which gives values of 0.1 to 1.0 cm/s for vegetated surfaces. An average value of 0.5 cm/s was used for this analysis. These are somewhat higher than particle deposition velocities measured at other forested sites (0.1 to 0.2 cm/s)[49]. Uncertainties in deposition velocities are estimated to be a factor of two. Wet deposition is neglected in this budget, but is not expected to dominate given the relatively low precipitation during the measurement period.

Data availability. The data that support the findings of this study are available from the corresponding author upon reasonable request.

638 **References only in Methods**

639

640 32. Faulhaber, A. E. *et al.* Characterization of a thermodenuder-particle beam mass
641 spectrometer system for the study of organic aerosol volatility and composition. *Atmos.*
642 *Meas. Tech.* **2,** 15–31 (2009).

643 33. Bahreini, R. *et al.* Organic aerosol formation in urban and industrial plumes near Houston
644 and Dallas, Texas. *J. Geophys. Res.* **114,** D00F16 (2009).

645 34. Stark, H. *et al.* Methods to extract molecular and bulk chemical information from series of
646 complex mass spectra with limited mass resolution. *Int. J. Mass Spectrom.* **389,** 26–38
647 (2015).

648 35. Lopez-Hilfiker, F. D. *et al.* Phase partitioning and volatility of secondary organic aerosol
649 components formed from α-pinene ozonolysis and OH oxidation: the importance of
650 accretion products and other low volatility compounds. *Atmos. Chem. Phys.* **15,** 7765–
651 7776 (2015).

652 36. Isaacman-VanWertz, G. *et al.* Ambient Gas-Particle Partitioning of Tracers for Biogenic
653 Oxidation. *Environ. Sci. Technol.* **50,** 9952–9962 (2016).

654 37. Stark, H. *et al.* Impact of thermal decomposition on thermal desorption instruments:
655 advantage of thermogram analysis for quantifying volatility distributions of organic
656 species. *Environ. Sci. Technol.* **In press.,** (2017).

657 38. Yatavelli, R. L. N. *et al.* Estimating the contribution of organic acids to northern
658 hemispheric continental organic aerosol. *Geophys. Res. Lett.* **42,** 6084–6090 (2015).

659 39. Yatavelli, R. L. N. *et al.* Semicontinuous measurements of gas–particle partitioning of
660 organic acids in a ponderosa pine forest using a MOVI-HRToF-CIMS. *Atmos. Chem.*

Phys. **14,** 1527–1546 (2014).

40. Kaser, L. *et al.* Comparison of different real time VOC measurement techniques in a ponderosa pine forest. *Atmos. Chem. Phys.* **13,** 2893–2906 (2013).

41. Cappellin, L. *et al.* On Quantitative Determination of Volatile Organic Compound Concentrations Using Proton Transfer Reaction Time-of-Flight Mass Spectrometry. *Environ. Sci. Technol.* **46,** 2283–2290 (2012).

42. Chan, A. W. H. *et al.* Speciated measurements of semivolatile and intermediate volatility organic compounds (S/IVOCs) in a pine forest during BEACHON-RoMBAS 2011. *Atmos. Chem. Phys.* **16,** 1187–1205 (2016).

43. Fry, J. L. *et al.* Observations of gas- and aerosol-phase organic nitrates at BEACHON-RoMBAS 2011. *Atmos. Chem. Phys.* **13,** 8585–8605 (2013).

44. US EPA. Estimation Programs Interface Suite™ for Microsoft® Windows 8. (2015).

45. Donahue, N. M. *et al.* Why do organic aerosols exist? Understanding aerosol lifetimes using the two-dimensional volatility basis set. *Environ. Chem.* **10,** 151 (2013).

46. Donahue, N. M., Robinson, A. L. & Pandis, S. N. Atmospheric organic particulate matter: From smoke to secondary organic aerosol. *Atmos. Environ.* **43,** 94–106 (2009).

47. DiGangi, J. P. *et al.* First direct measurements of formaldehyde flux via eddy covariance: implications for missing in-canopy formaldehyde sources. *Atmos. Chem. Phys.* **11,** 10565–10578 (2011).

48. Zhang, L., Gong, S., Padro, J. & Barrie, L. A size-segregated particle dry deposition scheme for an atmospheric aerosol module. *Atmos. Environ.* **35,** 549–560 (2001).

49. Farmer, D. K. *et al.* Chemically Resolved Particle Fluxes Over Tropical and Temperate

683 Forests. *Aerosol Sci. Technol.* **47,** 818–830 (2013).

SUPPORTING INFORMATION

for

Comprehensive characterization of atmospheric organic carbon at a forested site

James F. Hunter, Douglas A. Day, Brett B. Palm, Reddy L. N. Yatavelli, Arthur W. H. Chan, Lisa Kaser, Luca Cappellin, Patrick L. Hayes, Eben S. Cross, Anthony J. Carrasquillo, Pedro Campuzano-Jost, Harald Stark, Yunliang Zhao, Thorsten Hohaus, James N. Smith, Armin Hansel, Thomas Karl, Allen H. Goldstein, Alex Guenther, Douglas R. Worsnop, Joel A. Thornton, Colette L. Heald, Jose L. Jimenez, Jesse H. Kroll

Quality control.

The data from many of the instruments consist of 2D matrices with both large numbers of time points as well as large numbers of individual compounds. Because many of the individual ions that are measured correspond to compounds that are unidentified, some quality control of the data was required that is independent of molecular identity. A basic screen was applied to all the time series to eliminate features that are likely non-physical or associated with instrument background or electronic interference (e.g. signal spikes). Approximately 1% of the time points were excluded.

Classes of organic species not measured by this instrument suite.

The instrumentation suite measures most known classes of atmospheric organic species, including oligomeric species in the aerosol phase, which are detected by both the AMS and the MOVI-CIMS[1,2]. The main organic classes which are not measured by any of the five instruments

are volatile reduced species, namely $C_{\leq 13}$ alkanes and $C_{\leq 4}$ alkenes, and gas-phase ELVOCs, which condense on particles rapidly after formation and so are present in only very small concentrations. It is also possible that some functionalized (non-acidic) IVOCs may not be detected efficiently by the instrument suite; such compounds can in principle be detectable by the PTR-MS and TD-EIMS, but may be lost to inlet surfaces (PTR-MS) or undergo thermal decomposition (TD-EIMS) prior to mass spectrometric detection.

Rate coefficients used in reaction rate calculations.

The literature rate coefficients used in this study are presented in Table S1. All values were obtained from the Master Chemical Mechanism (v3.3)[3,4] (http://mcm.leeds.ac.uk/MCM), which in turn were generally obtained from IUPAC recommendations[5]. All the rates were calculated for a temperature of 20 °C for simplicity. This value is marginally higher than the measured mean temperature (17.5 °C), leading to only a small difference in the calculated rates. Photolysis rates were calculated as a function of diurnal hour for solar zenith angles from the midpoint of the campaign and subsequently averaged.

Table S1. Rate coefficients used in this study.

Compound	O_3 Rate Coefficient (cm^3 $molec^{-1}$ s^{-1})	OH Rate Coefficient (cm^3 $molec^{-1}$ s^{-1})	NO_3 Rate Coefficient (cm^3 $molec^{-1}$ s^{-1})	Photolysis rate (s^{-1})
Formaldehyde	-	8.50E-12	-	2.83E-05
Methanol	-	9.00E-13	-	-
Acetaldehyde	-	1.50E-11	-	1.35E-06
Formic Acid	-	4.50E-13	-	-
Ethanol	-	3.20E-12	-	-
Acetone	-	1.05E-13	-	5.9E-06
Acetic Acid	-	8.00E-13	-	-
Isoprene	1.27E-17	1.00E-10	-	-
Methacrolein	1.22E-18	2.90E-11	-	6.31E-06

Methylglyoxal	-	1.30E-11	-	5.35E-05
MEK	-	1.10E-12	-	1.77E-05
Benzene	-	1.20E-12	-	-
MBO	1.00E-17	1.60E-10	1.10E-14	-
Toluene	-	5.70E-12	-	-
Xylene	-	2.31E-11	-	-
Monoterpenes	8.70E-17	5.25E-11	6.10E-12	-
Sesquiterpenes (avg)[a]	1.16E-14	1.6E-10	1.8E-11	-
Humulene	1.16E-14	2.93E-10	3.9E-11	-
Longifolene	0	4.7E-11	6.8E-13	-
Aromadendrene	6.5E-15	-	-	-
Alloaromadendrene	6.5E-15	-	-	-
Muurolene	9.7E-15	-	-	-

[a]The average rate coefficients for sesquiterpenes were calculated from TAG speciated sesquiterpene concentrations and associated rate coefficients. The ozone rate coefficient for aromadendrene was obtained from Pollman et al[6], and the coefficients for aromadendrene and muurolene were estimated to be 1x and 1.5x the rate of aromadendrene. These speciated sesquiterpenes make up about 10% of the total sesquiterpene signal from the PTR-MS. Photolysis rates are calculated and averaged for solar zenith angles corresponding to the middle of the campaign.

Uniformity of concentrations over the entire campaign.

The values reported in this work reflect campaign averages for instruments, each of which had somewhat different measurement periods. Combining them into a single campaign average is reasonable given the relatively uniform time series, in which approximately the same concentrations and diurnal patterns were measured day to day for all instruments. Figure S1 shows the full time series for two major organic types, monoterpenes (panel a, from PTR-MS measurement) and OA (panel b, from AMS measurements), plotted diurnally such that the overall variability is apparent. Monoterpenes are highly reactive and have highly variable emissions, and therefore should give an upper limit to the amount of variability within the

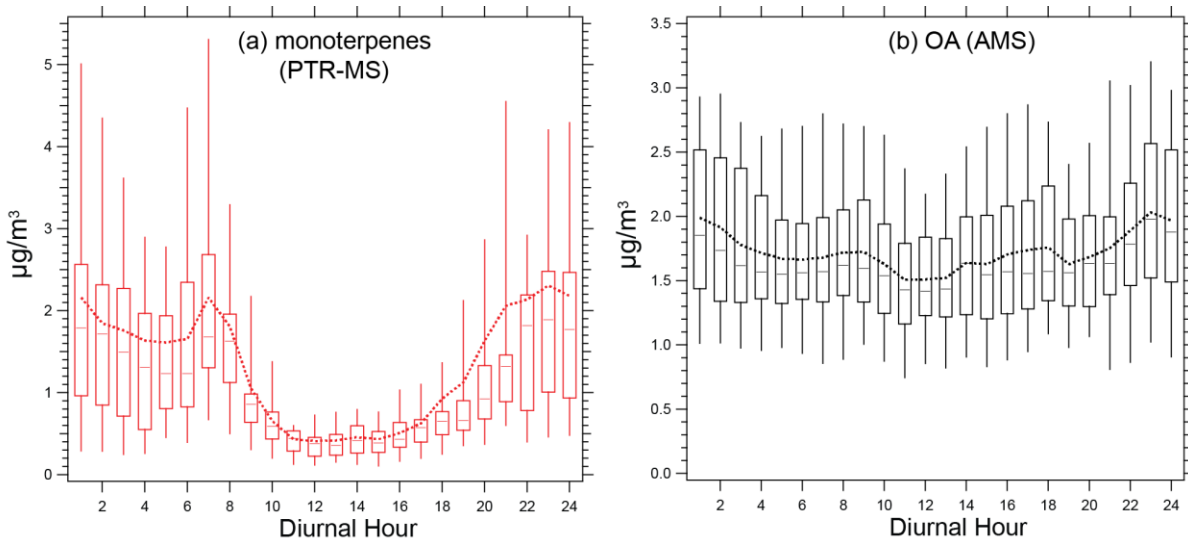

Figure S1. Variability of measured species during BEACHON-RoMBAS, illustrated by the campaign time series of summed monoterpenes (panel a) and organic aerosol (panel b). The dashed line is the average, the whiskers extend to the 5th and 95th percentile, and the box contains the median bounded by the 25th and 75th percentiles. The variability is approximately a factor of two for both monoterpenes (short-lived) and organic aerosol (long-lived) with no significant departures from the average diurnal profile excepting a handful of points. This suggests that the chemistry was similar day-to-day, and supports the comparison of average data from instruments in this study that had somewhat different sampling periods.

dataset. OA is much longer lived, and should give a lower limit to the variability due to day to day differences in chemistry. Both quantities have approximately a factor of two spread in their concentrations, with the exception of a few much higher points for monoterpenes (which do not significantly impact the overall average); further, no obvious campaign-wide trends are seen in either dataset. This indicates that there were no significant departures from campaign-averaged chemistry during the campaign, supporting the use of overall diurnal averages, and allowing for comparisons of measurements taken over somewhat different periods. The concentrations and calculated fluxes also vary over the course of the day, but these differences do not significantly change the overall conclusions, and a 24-hour average is therefore used throughout the text (except for in the discussion of diurnal cycles, below). The uniformity of the time series gives

confidence in the comparability of the data sets from the five instruments in this study in spite of the differences in their collection periods.

Estimates of vertical mixing time.

Approximate estimates of the mixing time can be constructed from the roughness velocity (u*) and Monin-Obukhov length (L, a measure of atmospheric stability) available for the field site, which enable the calculation of the vertical eddy diffusion coefficient (K_{zz})[7]; the mixing timescale is calculated by dividing K_{zz} by the square of the boundary layer height. The diurnally-averaged timescale ranges from 8 minutes during midday (when convection is strong) to a maximum of 6.3 hours at night (when the boundary layer is stable). Because K_{zz} is expected to change with changing height, this estimate constructed from the surface-layer sonic measurements may not accurately describe the overall mixing time. However, the mixing time during the day can also be estimated using the convective velocity w* (approximately 1 m/s [7]), resulting in a time of about 18 minutes. This is reasonably comparable to the value calculated using the M-O methods, and suggests these estimates of mixing times are reasonable.

Diurnal trends.

Diurnal trends for the campaign are shown in Figure S2 and S3. Such trends can result from a number of factors, including changes to emissions (which in turn depend on temperature, and, in some cases, light), oxidant levels, transport, vertical mixing, and boundary layer height. Figure S2a shows average diurnal profiles in temperature and photosynthetically active radiation (PAR) for the campaign (1 July to 27 Aug); both increase at the same time starting around 6 h,

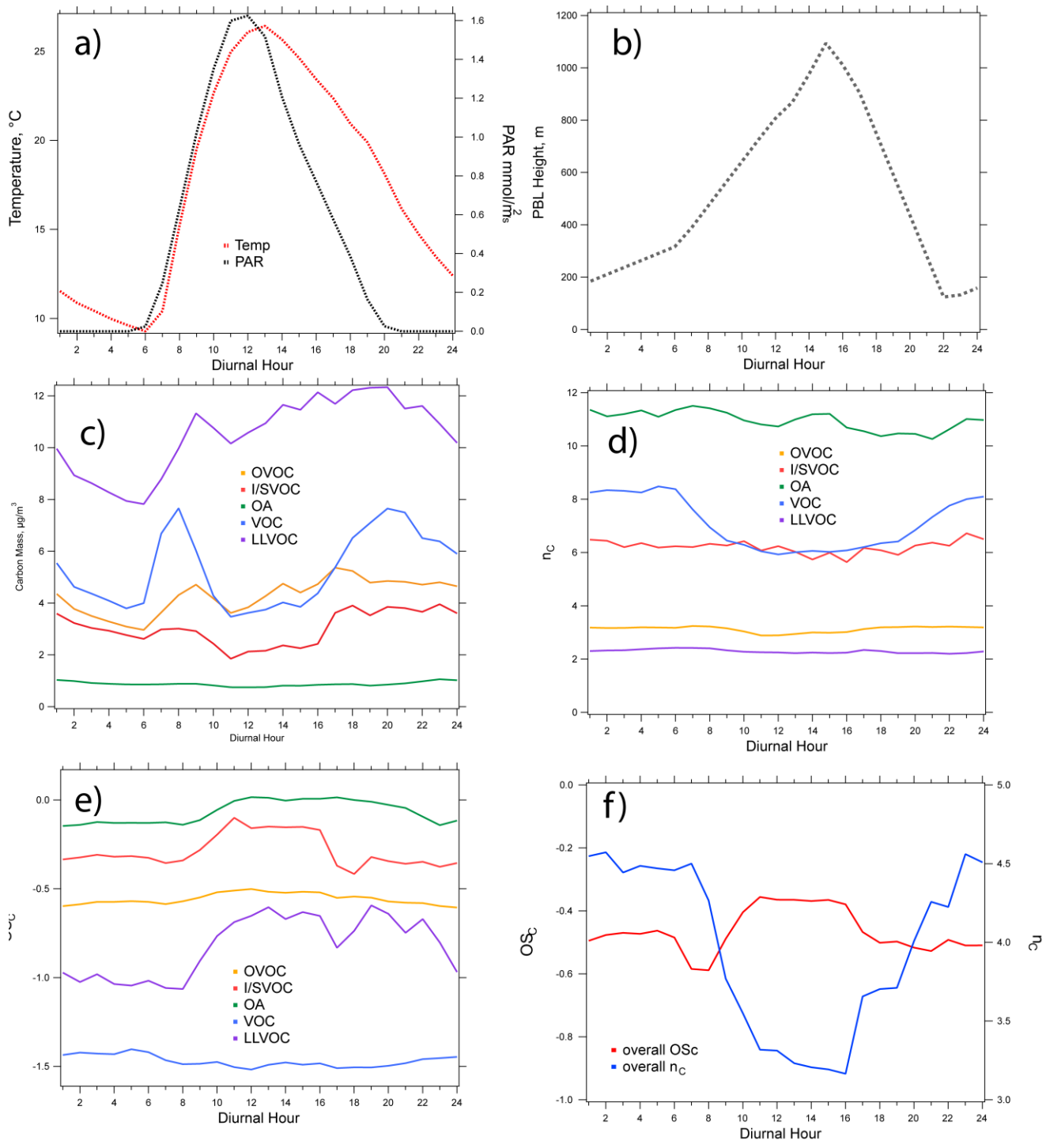

Figure S2: Campaign-average diurnal trends. Panel a: temperature and PAR; b: boundary layer height; c: concentrations of organic carbon for each organic class; d: carbon-weighted n_C for each class; e: carbon-weighted $\overline{OS}_C$ for each class; f: average n_C and $\overline{OS}_C$ for all measured organic carbon.

90

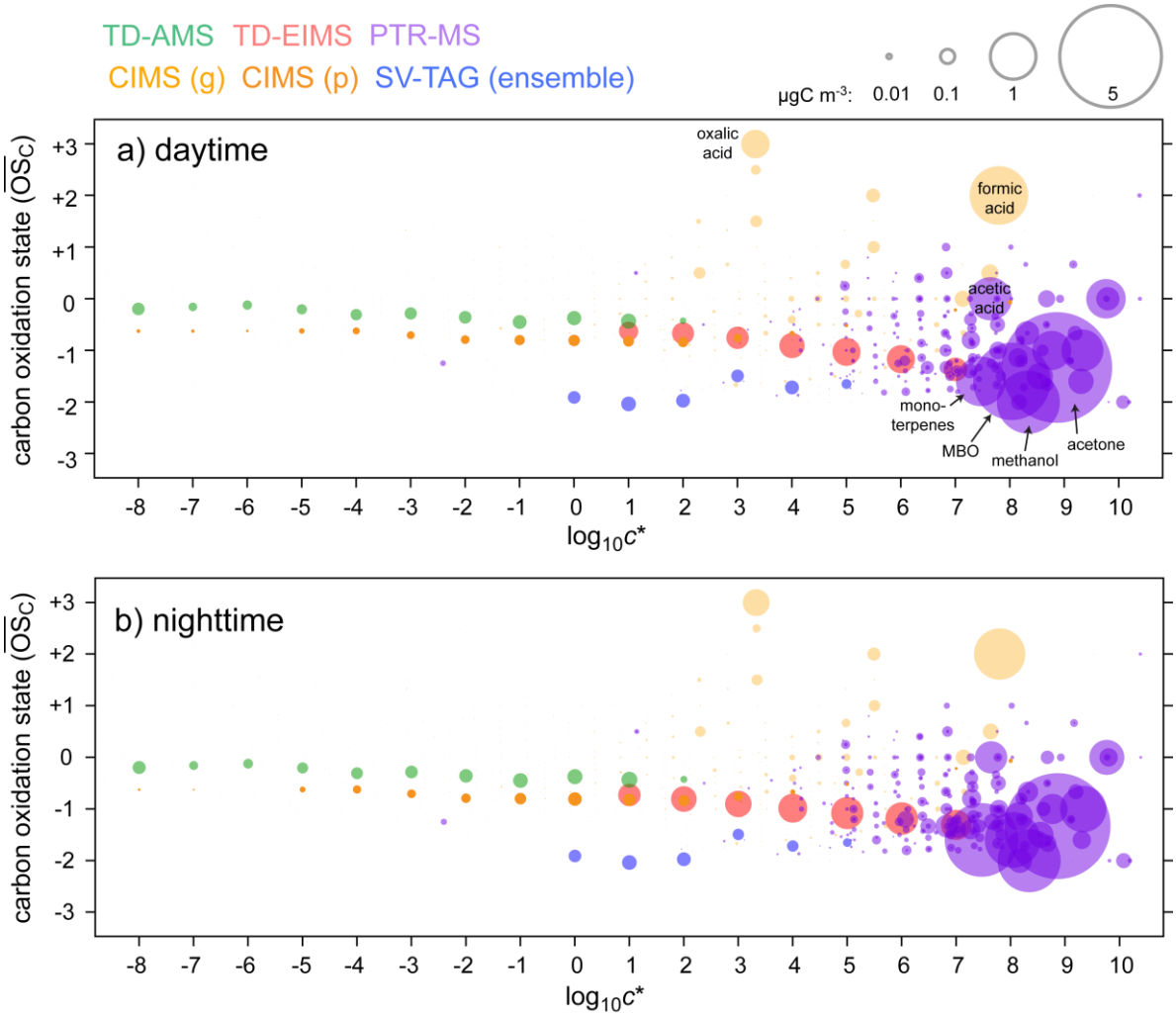

Figure S3: Average 2DVBS distributions of ambient organic species measured during the daytime (panel a, 06:00 to 17:00) and nighttime (panel b, 18:00 to 05:00). Day-night differences are consistent with the diurnal plots in Fig. S2. Differences include substantially higher levels of MBO (due to higher emissions), higher levels of formic and acetic acids (due to higher emissions and/or photochemical formation), and lower levels of monoterpenes (due to the higher boundary layer) during the daytime. Additionally monoterpene and S/IVOC levels are higher during the nighttime, possibly due to the low boundary layer and the lack of photochemical sinks.

with with temperature reaching a maximum of 26°C (from a low of 9°C) around 13 h. Light intensity reaches a maximum slightly earlier, and decreases much more rapidly than does temperature. This leads to emissions of temperature- and light-dependent compounds increasing sharply together in the morning, and temperature-driven emissions (e.g., some monoterpenes) persisting longer than compounds with strong light-dependent emissions (e.g., MBO) in the afternoon. The resulting concentrations are also a strong function of the boundary layer height

(S2b) and the intensity of photochemistry, both of which peak in midday; this can lead to lower concentrations even though emission rate of primary compounds and formation rates of secondary compounds are highest at this time.

Figures S2c-f and S3 show diurnal changes to the amounts and properties of the measured organic carbon. Figure S2c shows diurnal changes to each of the categories of organics; diurnal trends in carbon number (n_C) and oxidation state ($\overline{OS}_c$) for each category are given in Figs. S2d and S2e, respectively, and the average n_C and $\overline{OS}_c$ for all measured organic species are given in Figure S2f. VOC concentrations increase sharply in the morning with the onset of light-driven emissions (e.g. MBO) and to a smaller degree with increasing temperature-driven emissions (monoterpenes) into a shallow boundary layer. Concentrations decrease sharply in the late morning due to photooxidation and the boundary layer height increasing to an afternoon peak of about 1100 m. Concentrations rise again in the evening as photochemistry slows and temperature-driven emissions (e.g. monoterpenes) continue into a shrinking boundary layer (which eventually reaches a midnight minimum of about 100 m). This diurnal pattern of MBO and monoterpene emissions is reflected in Figure S3, as well as in the average carbon number for VOCs (Fig. S2d). Secondary, reactive species (OVOCs and S/IVOCs) behave similarly, but with somewhat delayed profiles due to their formation from oxidation processes. The long-lived VOCs show substantial variability over the course of the day, indicating their sources (emissions, secondary formation, influx) and sinks (efflux) are important over these timescales, even though oxidative loss is not. This lack of oxidation explains why their concentrations remain high throughout the afternoon, with no characteristic dip. Diurnal changes in LL-VOCs are driven by increases in acetone and formic acid (by emissions and/or secondary production) during the daytime; these increases lead to the large increase in $\overline{OS}_c$ (but no change

to n_C) over the daylight hours. OA stays relatively constant over the course of the day, with a distinct increase in $\overline{OS}_c$ during the daytime (which is also reflected in the $\overline{OS}_c$ of S/IVOCs), possibly indicating more intense oxidation (aerosol aging or formation of more-oxidized SOA) during this time.

Lower-limit calculations of organic carbon distributions.

The distributions of organic carbon provided in the text (Figs 1c-e, 2, and 3) all assume no overlap between the carbon measured by different instruments (except in unambiguous cases of overlap), providing an upper limit for the amount of carbon measured. The specific areas of overlap that are accounted for in the upper limit case are: AMS and CIMS particle phase (for which the AMS measurement is used), formic acid in the PTR-MS and CIMS (for which CIMS measurement is used), and sesquiterpenes in the TAG and PTR-MS (for which the PTR-MS measurement is used). The corresponding lower limits in carbon concentrations, in which maximal overlap is assumed, are shown in Figure S4. Results are not dramatically different than those from the upper-limit calculation: the total loading is reduced by 4.1 μg/m^3 (15%), with the largest differences being the loadings of S/IVOCs (since they are measured by the most instruments). In almost all cases these such upper-limit/lower-limit differences (including in individual "bins" in Figs. 1 and S4) are smaller than measurement uncertainty (error bars). Thus the two cases agree to within error of the measurements, and details of the treatment of instrument overlap does not substantially affect conclusions about the overall amounts, properties, or reactivity of the measured organic species.

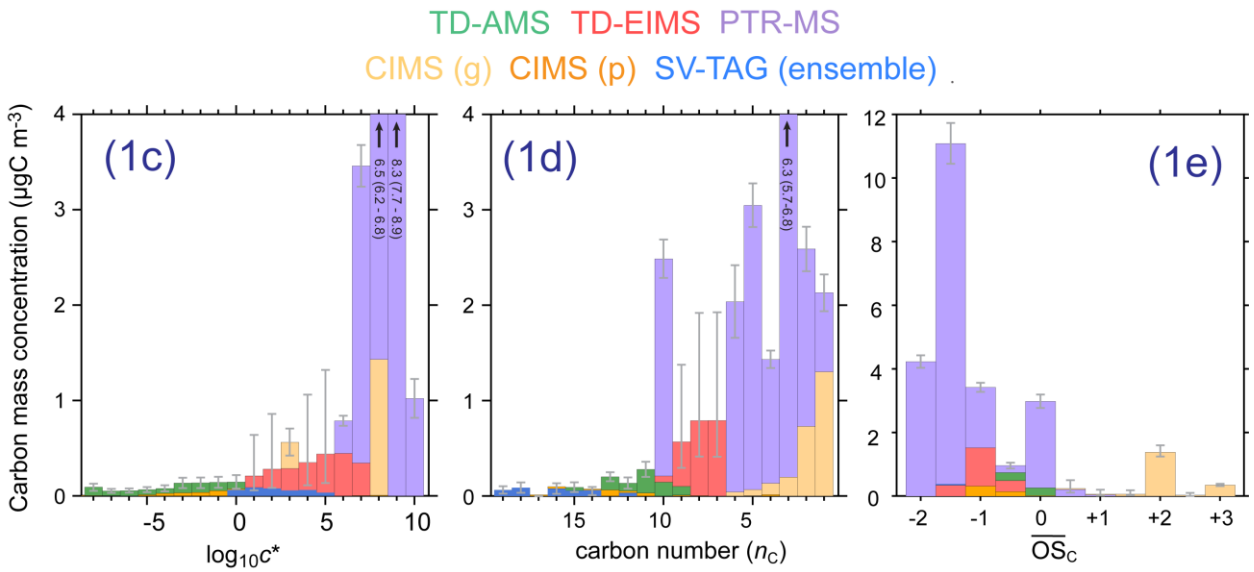

Figure S4: Lower-limit campaign-average carbon distributions, assuming maximum overlap among measurements from different instruments (so bars are overlain rather than stacked, as in the upper-limit case in Figure 1). Panel numbers give the corresponding upper-limit figure/panel number in the main text.

141

142 **Scaling of OH reactivity by emissions.**

143 OH reactivity was not measured in 2011, but were measured the previous year as part of the
144 BEACHON-ROCS campaign[8]. In order to extrapolate the 2010 OH reactivity to 2011, the
145 differences in estimated emissions of the species primarily responsible for OH reactivity were
146 used. These differences in emissions are themselves calculated from differences in the known
147 temperature and PAR and the equations given in Kaser et al.[9] for temperature- and light-
148 dependent emissions of BVOCs. MBO and monoterpenes are the two largest sources of OH
149 reactivity (59% of the total), and are the only significant sources of OH reactivity for which
150 emissions measurements are available. Therefore, the year-to-year difference in emissions for
151 these species only were used to calculate the scaling factor for OH reactivity. The 2011 OH
152 reactivities for MBO and monoterpenes were normalized by their 2011 emissions, and the
153 resulting factors used to calculate the 2010 MBO and monoterpene OH reactivities. These were
154 then scaled proportionally such that their sum was equal to the 2010 measured value for total OH

reactivity (10 s^{-1}). These scaled OH reactivities were then multiplied by the 2010-11 fractional changes in emissions to estimate the 2011 total reactivity (8 s^{-1}). Although emissions of monoterpenes and other BVOCs increased from 2010 to 2011, the relative contribution of MBO to the OH reactivity is so much larger that its decrease from 2010 to 2011 dominates the overall change.

SOA formation estimates.

For all known/studied SOA precursors, the SOA yields, OM/OC values, and carbon yields (equal to SOA yield divided by OM/OC), along with references for each, are given in Table S2. To ensure proper comparison with the oxidation flow reactor (OFR) measurements, these include only measurements from experiments in which RO_2 chemistry is dominated by reaction with HO_2, with no influence from aqueous-phase uptake, etc. Relative error for carbon yields is estimated to be 30%. For unknown/unmeasured species (unspeciated (O)VOCs and all I/SVOCs except sesquiterpenes), yields are estimated from the c^* of the precursor species, using the general approach of Donahue et al.[10] The functional form used is shown in Figure S5; error in this approach is likely high, conservatively assumed to be a factor of three (indicated by shaded grey region in Figure S5). Note that the resulting range includes the strict upper limit of a 100% carbon yield for low-volatility species.

Table S2. Aerosol yields used in this study.

SOA precursor	Aerosol yield (c_{OA} = 1.8)	OM/OC	Aerosol carbon yield
Sesquiterpenes	13.2%[a]	1.47[d]	9.0%
Methacrolein	2.4%[b]	1.87[b]	1.3%
Isoprene	3.2%[a]	1.91[b]	1.7%
Toluene	13.8%[a]	2.0[b]	6.9%
Xylene	21.6%[c]	2.1[b]	10.3%
Monoterpenes	12.5%[a]	1.7[b]	7.4%

[a]Palm et al 2016,[11] [b]Chhabra et al 2011,[12] [c]Loza et al 2012,[13] [d]Tasoglou et al 2015.[14]

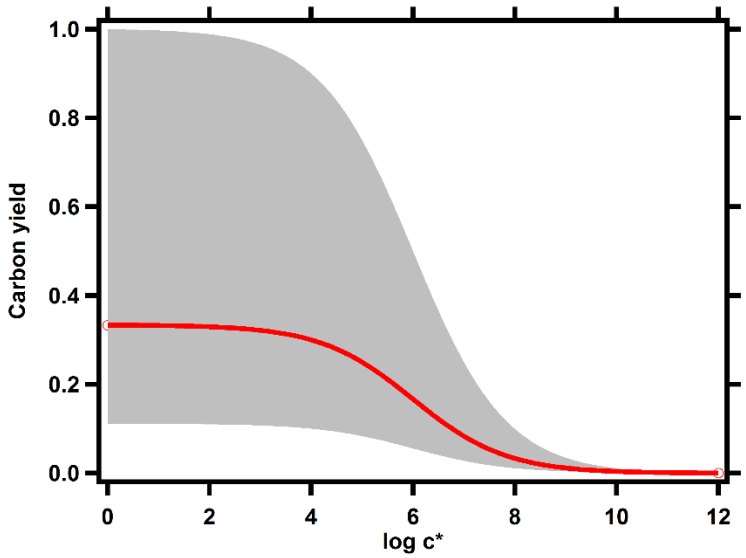

Figure S5: Functional form used to estimate aerosol yields for unspeciated compounds similar to the method used in Donahue et al.[10] Grey shaded region indicates range of a factor of three in estimated yields.

SOA formation measurement.

A detailed description of the OFR measurements during this field study can be found in Palm et al.[11]; a brief summary is presented here. *In situ* SOA formation was measured by the AMS and a scanning mobility particle sizer (SMPS) after OH oxidation of ambient air inside the OFR. The maximum amount of SOA formation was observed after 0.4–1.5 equivalent days of OH aging (assuming a typical ambient OH concentration of 1.5 x 10^6 molec m^{-3})[15]. On average in this photochemical age range, 0.93 μgC m^{-3} SOA (2.4 μg m^{-3} total SOA) was formed from the precursors in ambient air. This number includes a correction to account for the fate of condensable organic vapors in the OFR (referred to as the "LVOC fate correction" in Palm et al., 2016)[11]. When LVOCs are formed by oxidation in the OFR, they can have several fates, including condensing on existing particles to form SOA, condensing on the internal OFR walls

(similar to chamber wall losses)[16], being oxidized again prior to condensation leading to volatile fragmentation products, or exiting the OFR to condense rapidly on sampling line walls. The latter three fates do not result in SOA formation. In the atmosphere, the dominant fate of such condensable gases is condensation onto aerosols to form SOA[17–19]. This correction is thus applied in order to relate the OFR measurements to what would occur in the atmosphere. This model was verified using sulfate aerosol formation from SO_2 during this study[11]. The average overall correction factor is 1.8x.

TD-EIMS calibration and analysis.

The specific instrumental calibration and analysis procedures used in the BEACHON-RoMBAS field campaign are discussed in detail elsewhere for all instruments[11,20–22] with the exception of the TD-EIMS. The TD-EIMS instrument is described by Cross et al.[23], but a set of new calibration and data-processing routines were developed for the present campaign; these are discussed in this section.

Mass concentration calibration. To compute the total mass of S/IVOCs in a given mass spectrum, the sum of organic ion counts for a given data point was computed, and an analogous sum computed for a measurement of background signal (zero air). For unit-mass resolution data, organic signal was separated from inorganic signal by applying a filter to the data to exclude ions at mass-to-charge ratios that are primarily inorganic (e.g., *m/z* 28, 32, 40, 44). The background signal was subtracted from the sample signal, and the difference in ion counts was multiplied by an empirically measured proportionality constant to convert to total mass. This empirical measurement was performed by vaporizing a compound (*n*-hexadecane or α-pinene) at a known rate into the sample gas stream using a syringe pump or diffusion cell. For the syringe pump, the

flow rate and infusion rate were both known, permitting an accurate calculation of gas phase concentration. The diffusion cell was a capillary coated with a given calibrant; pressure was then applied to one end of the capillary, resulting in a controlled flow of saturated vapor, at the rate measured using a flow-meter, or calculated using Poiseuille's equation. Calibrations were performed using at least three gas phase concentrations to check for linearity. A typical calibration plot taken during the campaign is shown in Figure S6a. Laboratory calibrations have found the observed linearity to extend to even lower concentrations.

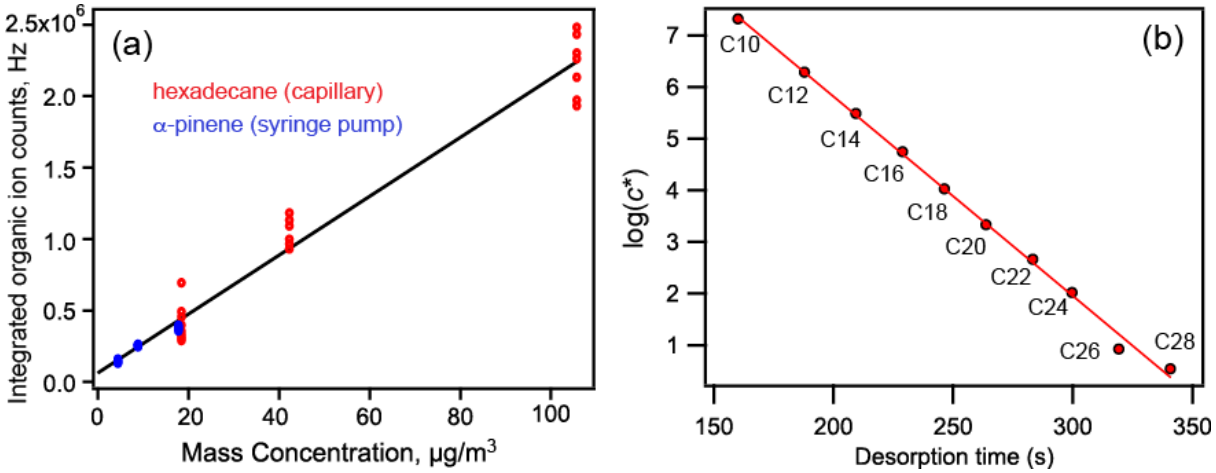

Figure S6: Sample TD-EIMS calibration runs. Panel a: calibration for determining organic mass from organic ion counts. Known concentrations were introduced into the instrument using a diffusion cell for hexadecane and a syringe pump for α-pinene. The calibration constant (slope) incorporates the collection and transmission efficiency, which is the same for both molecules for the sampling parameters used during calibration. Panel b: Volatility calibration, relating *c** to desorption times, using a standard *n*-alkane mixture. The known saturation vapor concentrations of these molecules can be interpolated with a linear fit, yielding an estimate of volatility for material desorbing at any time/temperature.

Volatility calibration. To compute S/IVOC mass as a function of volatility, individual desorptions are split into bins computed using measured a standard mixture of *n*-alkanes (C_{10}-C_{28}) with known saturation vapor pressures. The relationship between desorption time and log(*c**), shown in Fig. S6b, is linear; because the temperature ramp is itself linear, equivalent bin boundaries can be drawn in both temperature and time space. Conversion to *c** bins involves

integrating between the boundaries and subtracting an appropriate background (discussed further below). The measured desorption times/temperatures are likely a function of the sorption characteristics as well as the vapor pressure of a given molecule, and therefore the reported c^* values are in alkane-equivalent volatilities.

Processing routines for high-resolution mass spectrometric data. The data analysis procedures for the TD-EIMS use the Squirrel and Pika modules (http://cires1.colorado.edu/jimenez-group/wiki/index.php/ToF-AMS_Analysis_Software). Separation of organic and inorganic ions is greatly simplified, since individual ions can be quantified within a single nominal mass (e.g. CO_2^+ and $C_2H_4O^+$ at m/z = 44). Since the composition of individual ions is known, elemental analysis is possible by summing the total signal for carbon, hydrogen, oxygen and nitrogen for all ions, a procedure that has been described in the literature[24]. The correction factors described in Aiken et al. (accounting for systematic undercounting of oxygen due to electronegativity) have not been measured for the TD-EIMS. The TD-EIMS is also unable to quantify CO_2^+ due to significant gas-phase interference. Together, these two effects likely lead to an estimate of the O/C that may be biased somewhat low. Elemental analysis is performed using the same approach for summation and background subtraction as the determination of organic mass, described below.

Background subtraction. Background subtraction procedures involve the subtraction of an appropriate thermogram for an S/IVOC-free air sample (zero air). Blank thermograms are taken at least twice a day to check for zero-drift and the possibility of accumulation of low-volatility material. At least two blank desorption runs are taken in succession in order to assess variability. Blank subtraction was performed in time space during BEACHON-RoMBAS. Several additional steps are necessary to maximize the quality of the resulting data, shown in

Figure S7. The first is that the tungsten filament is subject to rapid erosion, significantly increasing emission current over the course of the day, and thereby affecting the ionization efficiency (number of ions produced per microgram of sample). To counteract this, a calibration for signal as a function of emission current was performed (Figure S7a), and the fit function used to normalize all data points to an emission current of 1.0 mA (matched to the value used for the mass calibration). The second is that the signal intensity fluctuates from desorption to desorption independently of the emission current and independently of the total organic loading. The initial part of each desorption is entirely due to air ions, and should be essentially identical in all desorptions. Sample desorptions are therefore normalized such that the air signal matches that of the blank desorption, shown in Figure S7b, region 1. These corrections are on the order of 5%. The last issue is that due to irregularities in the triggering and recording of mass spectra, the desorptions have a small random offset of up to 5 seconds. The offset is difficult to separate from real differences in the desorption, and can lead to large changes in the apparent volatility distribution if not accounted for, especially around sharp peaks (see Figure S7b, region 2). We use siloxanes as an internal standard due to their narrow peak shape and consistent profile, allowing for the correction for the time offset (Figure S7c). By correlating *m/z* 73 (dominated by siloxanes) for the sample and blank desorptions, and applying a peak finding routine to the resulting profile (Figure S7d), the offset can be determined and applied to the blank run, allowing for an accurate background subtraction (black curve in Figure S7b). Differences between signal in different background measurements (summed across all volatility bins) was on the order of 0.1 $\mu g/m^3$, so are unlikely to affect averaged results.

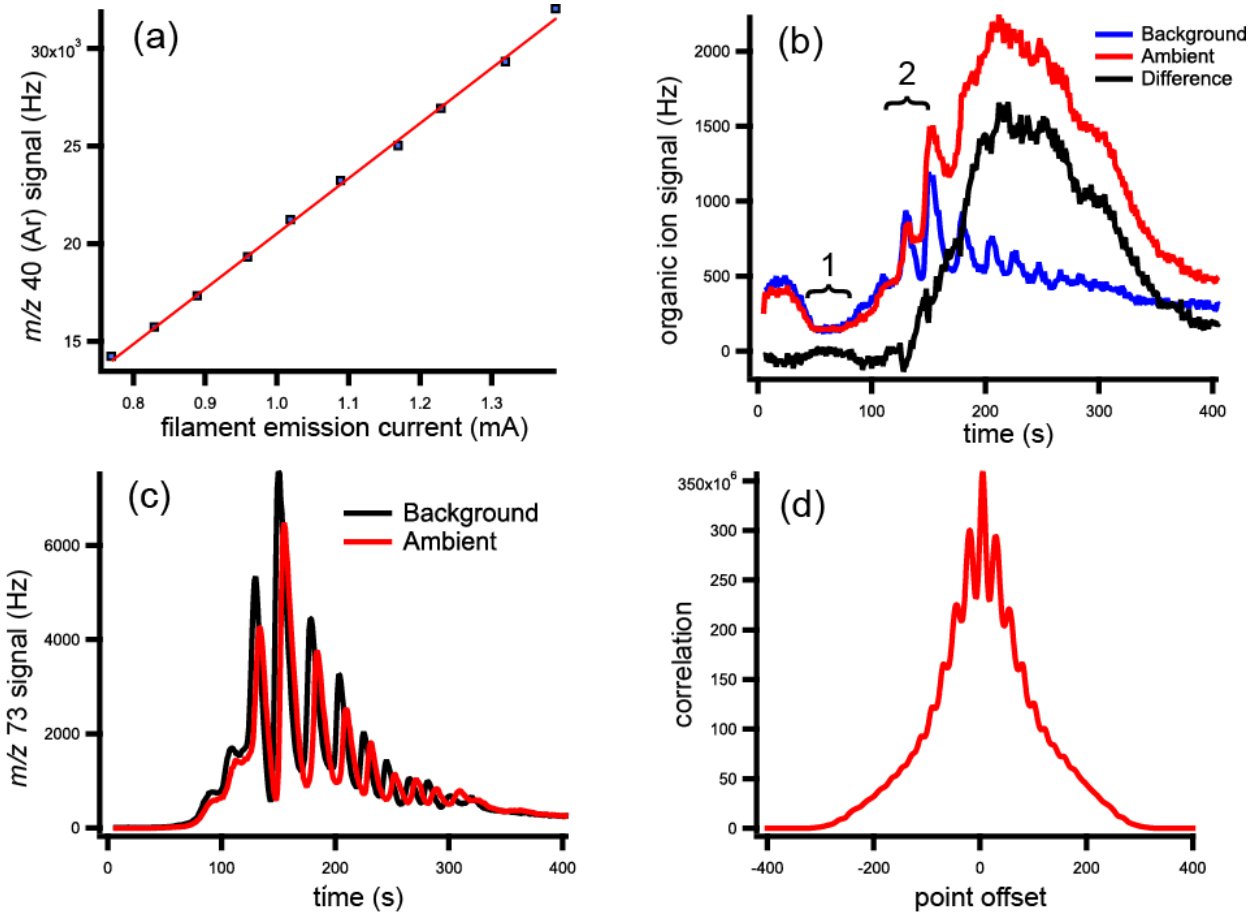

Figure S7: Details of TD-EIMS background subtraction. Panel a: differences in filament emission current over time are compensated for using the argon signal calibration shown. Panel b: a measured background desorption (blue curve) is normalized to a part of the ambient desorption (red curve) containing mostly inorganic ions (region 1). Panel c: Differences in run-to-run desorption times are found using siloxanes (*m/z* 73) as an internal standard. Panel d: the convolution of *m/z* 73 between background and ambient desorptions gives the time offset necessary to optimize background subtraction (black curve in panel b).

References.

1. Kroll, J. H., Ng, N. L., Murphy, S. M., Flagan, R. C. & Seinfeld, J. H. Secondary Organic Aerosol Formation from Isoprene Photooxidation. *Environ. Sci. Technol.* **40,** 1869–1877 (2006).

2. Lopez-Hilfiker, F. D. *et al.* Phase partitioning and volatility of secondary organic aerosol components formed from α-pinene ozonolysis and OH oxidation: the importance of accretion products and other low volatility compounds. *Atmos. Chem. Phys.* **15,** 7765–7776 (2015).

3. Saunders, S. M., Jenkin, M. E., Derwent, R. G. & Pilling, M. J. Protocol for the development of the Master Chemical Mechanism, MCM v3 (Part A): tropospheric degradation of non-aromatic volatile organic compounds. *Atmos. Chem. Phys.* **3,** 161–180 (2003).

4. Jenkin, M. E., Saunders, S. M., Wagner, V. & Pilling, M. J. Protocol for the development of the Master Chemical Mechanism, MCM v3 (Part B): tropospheric degradation of aromatic volatile organic compounds. *Atmos. Chem. Phys.* **3,** 181–193 (2003).

5. Atkinson, R. *et al.* Evaluated kinetic and photochemical data for atmospheric chemistry: Volume II - gas phase reactions of organic species. *Atmos. Chem. Phys.* **6,** 3625–4055 (2006).

6. Pollmann, J., Ortega, J. & Helmig, D. Analysis of Atmospheric Sesquiterpenes: Sampling Losses and Mitigation of Ozone Interferences. *Environ. Sci. Technol.* **39,** 9620–9629 (2005).

7. Seinfeld, J. H. & Pandis, S. N. *Atmospheric Chemistry and Physics: From Air Pollution to Climate Change*. (Wiley Interscience, 2006).

8. Kim, S. *et al.* Evaluation of HOx sources and cycling using measurement-constrained model calculations in a 2-methyl-3-butene-2-ol (MBO) and monoterpene (MT) dominated ecosystem. *Atmos. Chem. Phys.* **13,** 2031–2044 (2013).

9. Kaser, L. *et al.* Undisturbed and disturbed above canopy ponderosa pine emissions: PTR-TOF-MS measurements and MEGAN 2.1 model results. *Atmos. Chem. Phys.* **13,** 11935–11947 (2013).

10. Donahue, N. M., Robinson, A. L. & Pandis, S. N. Atmospheric organic particulate matter: From smoke to secondary organic aerosol. *Atmos. Environ.* **43,** 94–106 (2009).

11. Palm, B. B. *et al.* In situ secondary organic aerosol formation from ambient pine forest air using an oxidation flow reactor. *Atmos. Chem. Phys.* **16,** 2943–2970 (2016).

12. Chhabra, P. S. *et al.* Elemental composition and oxidation of chamber organic aerosol. *Atmos. Chem. Phys.* **11,** 8827–8845 (2011).

13. Loza, C. L. *et al.* Chemical aging of m-xylene secondary organic aerosol: laboratory chamber study. *Atmos. Chem. Phys.* **12,** 151–167 (2012).

14. Tasoglou, A. & Pandis, S. N. Formation and chemical aging of secondary organic aerosol during the β-caryophyllene oxidation. *Atmos. Chem. Phys.* **15,** 6035–6046 (2015).

15. Mao, J. *et al.* Airborne measurement of OH reactivity during INTEX-B. *Atmos. Chem. Phys.* **9,** 163–173 (2009).

16. Krechmer, J. E., Pagonis, D., Ziemann, P. J. & Jimenez, J. L. Quantification of Gas-Wall Partitioning in Teflon Environmental Chambers Using Rapid Bursts of Low-Volatility Oxidized Species Generated in Situ. *Environ. Sci. Technol.* **50,** 5757–5765 (2016).

17. Farmer, D. K. & Cohen, R. C. Observations of HNO3, ΣAN, ΣPN and NO2 fluxes: evidence for rapid HOx chemistry within a pine forest canopy. *Atmos. Chem. Phys.* **8,** 3899–3917 (2008).

18. Knote, C., Hodzic, A. & Jimenez, J. L. The effect of dry and wet deposition of

condensable vapors on secondary organic aerosols concentrations over the continental US. *Atmos. Chem. Phys.* **15,** 1–18 (2015).

19. Nguyen, T. B. *et al.* Rapid deposition of oxidized biogenic compounds to a temperate forest. *Proc. Natl. Acad. Sci.* **112,** E392–E401 (2015).

20. Karl, T. *et al.* Selective measurements of isoprene and 2-methyl-3-buten-2-ol based on NO^+ ionization mass spectrometry. *Atmos. Chem. Phys.* **12,** 11877–11884 (2012).

21. Yatavelli, R. L. N. *et al.* Semicontinuous measurements of gas–particle partitioning of organic acids in a ponderosa pine forest using a MOVI-HRToF-CIMS. *Atmos. Chem. Phys.* **14,** 1527–1546 (2014).

22. Chan, A. W. H. *et al.* Speciated measurements of semivolatile and intermediate volatility organic compounds (S/IVOCs) in a pine forest during BEACHON-RoMBAS 2011. *Atmos. Chem. Phys.* **16,** 1187–1205 (2016).

23. Cross, E. S. *et al.* Online measurements of the emissions of intermediate-volatility and semi-volatile organic compounds from aircraft. *Atmos. Chem. Phys.* **13,** 7845–7858 (2013).

24. Aiken, A. C., DeCarlo, P. F. & Jimenez, J. Elemental Analysis of Organic Species with Electron Ionization High-Resolution Mass Spectrometry. *Anal. Chem.* **79,** 8350–8358 (2007).